Structure–Fluid–Mineralization System of Jiadi Gold Deposit in Southwestern Guizhou, China

Zhuang Min [1,2], Wengao Zhang [2,*], Jiayong Pan [1], Zhenju Zhou [2], Hailong Huo [2] and Guangwen Huang [1]

[1] State Key Laboratory of Nuclear Resources and Environment, East China University of Technology, Nanchang 330013, China; minz@ecut.edu.cn (Z.M.); jypan@ecit.cn (J.P.); gwhuang1991@163.com (G.H.)

[2] Institute of Geomechanics, Chinese Academy of Geological Sciences, Beijing 100081, China; zhenjuzhou@126.com (Z.Z.); huohailong2012@163.com (H.H.)

[*] Correspondence: zhangwengao@cags.ac.cn

Abstract: The Jiadi gold deposit, situated in the Southwestern region of Guizhou, is a large-scale, recently discovered, basalt-hosted, and fine-grained disseminated gold deposit. This study has unveiled that the tectonic deformation of the Jiadi gold deposit can be categorized into four stages: the Late Paleozoic crustal uplift and brittle deformation (D1-deformation) stage; the Early Yanshanian NW-trending compressive ductile deformation (D2-deformation) stage; the Late Yanshanian NS-trending strike-slip fault (D3-deformation) stage; and the Himalayan EW-trending nappe structure (D4-deformation) stage. The outcomes of the C-O isotope analysis revealed that the fluid responsible for ore formation exhibits the attributes of magmatic water blended with meteoric water, and the metallogenic constituents primarily originate from a deep source. The formation of the Jiadi gold deposit occurred during the D2-deformation stage and extended to the D3-deformation stage. The D2-deformation stage induced hydrothermal activity and rock devolatilization, leading to the generation of CO_2-rich and low-salinity fluids. The D3-deformation stage, which is intimately associated with mineralization, can be classified into three stages: the pyrite stage; the smoky quartz stage; and the sulfide stage. The findings obtained from laser Raman spectroscopy indicate that the inclusions typically comprise CO_2, CH_4, N_2, and SO_2. These deep fluids ascended along the fault to the interlayer fracture zone during the D3-deformation stage. The alteration of the geochemical environment was accompanied by fluid immiscibility or boiling, resulting in the rapid precipitation of metallogenic materials.

Keywords: Jiadi gold deposit; structural geology; fluid geochemistry; mineralization

1. Introduction

The Southwestern region of Guizhou is a highly significant gold-producing area located in the "Golden Triangle" between the Yunnan, Guizhou, and Guangxi provinces. It can be divided into two facies geologically, the Youjiang continental platform and the fold belt basin [1]. The Youjiang platform is dominated by strata-bound orebodies, such as the Shuiyindong and Jiadi gold deposits [2–4], and the basin area is based on fault-controlled orebodies, such as the Lannigou and Yata gold deposits [5–7]. These two types of orebodies have been recognized in Nibao and Linwang gold deposits [8], and there are differences in the ore-controlling structures and ore-forming fluids [9]. Structure and fluid play a crucial role in the formation of gold deposits, as well as in the precipitation of metallic elements, which are the result of their coupling [10–12].

The Jiadi gold deposit is located in the Qinglong–Luoping metallogenic belt of Southwestern Guizhou; it is hosted by the Jiadi fold belt and thrust belt in the area of strong structures that are on the southeast flank of the Lianhuashan anticlinorium. It is the largest primary basalt-hosted gold deposit in Guizhou Province [4]. Previous studies have focused on the geological characteristics, mineral assemblage, and hydrothermal alteration of the

deposit [13,14]; in addition, there have been certain studies conducted on the fluid geochemistry, mineralogy, chronology, gold occurrence regularity of gold, etc. [15–18]. Based on the distribution of ore-forming elements and hydrothermal veins, it is proposed that deep ore-forming fluids migrate and deposit sequentially along intrusive breccia bodies, interlayer fractures, and steep microfractures [19]. However, the source of metallogenic materials and the characteristics of ore-forming fluids remains under discussion. Furthermore, little is known about the structure that controls the formation of the ore deposit. Based on a detailed structural analysis, combined with research methods, such as fluid inclusions and stable isotopes, this paper studies the structural deformation characteristics of the deposit and properties of ore-forming fluids in order to explore the mechanism of ore-forming fluid migration and metallogenic materials precipitation. Moreover, such a study can provide information on mineral exploration and scientific research in this area [20,21].

2. Geological Setting

　　The Youjiang Basin is situated at the junction of the Simao Block, the Cathaysia Block, and the Yangtze Block. It is located at the conjugation of the eastern Tethys tectonic domain and the western edge of the Circum Pacific tectonic domain [22]. The basin is roughly surrounded by the NE-trending Shizong–Mile Tectonic belt, the EW-trending Gejiu–Binyang Tectonic belt, and the NW-trending Ziyang–Nandan Tectonic belt (Figure 1a). The basin has undergone the evolutionary stage where the rift basin experiences continental margins, back-arc basins, back-arc foreland basins, and intermountain basins. It has experienced the process of early extensional rifting, as well as sedimentary, late orogenesis, and extensional uplift, which correspond to the extension, subduction, closure, and orogeny of the Paleo-Tethys Ocean, respectively [23,24]. During the Caledonian orogeny, the Yangtze Block and Cathaysia Block collided, forming the South China fold system. Sedimentary rocks, volcanic rocks, marine carbonate rocks, and siliceous rocks began to form during the Hercynian movement. The convergent plate was accompanied by the magmatic intrusion, continental crust uplift, and tectonic activity in the Indochina–Yanshanian region, resulting in the formation of intermountain basins through compression and the reformation of deposits during the Himalayan period [25].

　　The Maokou Formation (P_2m) consists of thick (bioclastic) limestone that is intercalated with chert clumps or bands, while the upper Permian Emeishan Basalt Formation ($P_3\beta$) is tholeiite with pyroclastic rocks [26]. The Lianhuashan anticline is a NE-trending monoclinic structure with a general southeast dip, and it starts from Puan County and ends at Shiqiao Town. The upper Devonian and Carboniferous layers make up its core, and its two flanks mostly expose the Maokou Formation of the Middle Permian and the Emeishan Basalt structures (Figure 1c). It is approximately 40 km long and 9–20 km wide. The fault structures are relatively developed, mainly along the NE-trending and NNE-trending areas, with the NNE-trending and EW-trending regions showing less frequent occurrences. The general strike of the Zhudong fault is consistent with the anticline (Figure 1b), implying a close relationship as most of the faults develop near the axis of the anticline and are mainly high-angle normal (strike-slip) faults and reverse faults. These faults are characterized by multi-stage interformational slides and intricate hydrothermal alterations [13].
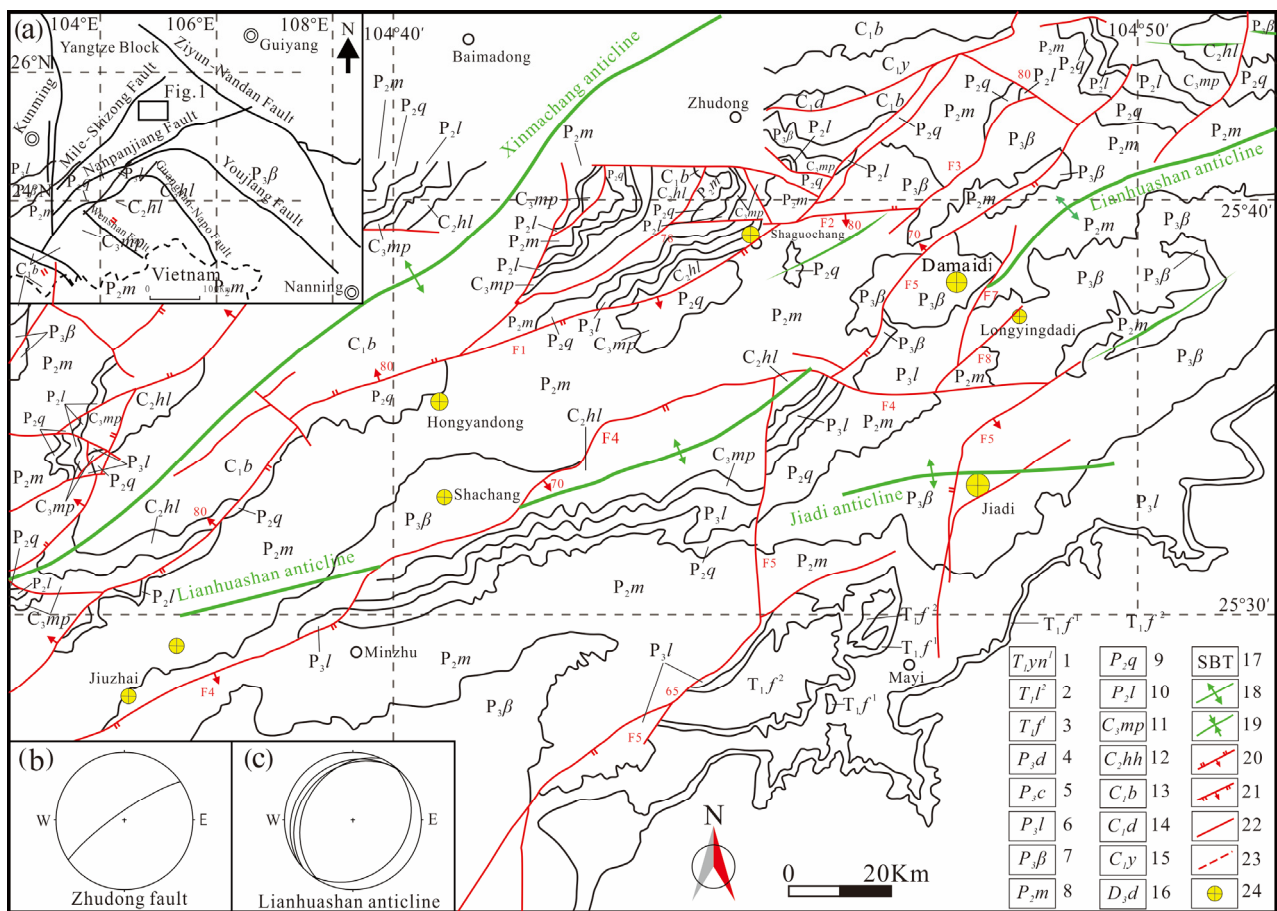
Figure 1. Schematic diagram of the geological structure of the Lianhuashan anticline and study area location map (modified from [13]) (**a**); the polar projection of the occurrence of the Zhudong fault (**b**); and the Lianhuashan anticlinal flanking strata (**c**). 1. First member of Yongningzhen Formation; 2. Second Member of Feixianguan Formation; 3. First member of Feixianguan Formation; 4. Dalong Formation; 5. Changxing Formation; 6. Longtan Formation; 7. Emeishan Basalt Formation; 8. Maokou Formation; 9. Qixia Formation; 10. Liangshan Formation; 11. Maping Formation; 12. Huanglong Formation; 13. Baozuo Formation; 14. Datang Formation; 15. Yanguan Formation; 16. Daihua Formation; 17. Structural alteration rock; 18. Synclinal axis; 19. Anticlinal axis; 20. Reverse faults; 21. Normal faults; 22. Uncertain fault; 23. Inferred faults; 24. Gold deposits (occurrence).

3. Geological Characteristics of Deposit

In the Jiadi gold deposit, the gray–black–light gray dolomitic limestone of P_2m is exposed. The gray–black massive microcrystalline basalt of $P_3\beta^3$ consists of gray–green basalt, basaltic volcanic breccia, as well as the tuff of $P_3\beta^2$ and $P_3\beta^1$. The deep-gray tuff, silty claystone, and siltstone of P_3l, P_2q, P_2l, and C_2mp occur locally in the northwest section of Jiadi Village, and the Q4 is widely distributed (Figure 2). The fault structures in the mining area are mainly NEE-trending and NNE-trending, with a few NS-trending and EW-trending. The NE-trending faults are represented by F101, F103, and F104 faults, with a strike extension of 600~4100 m. The fault zone is dominated by a poorly cemented fault breccia with complex composition, common striation, step-on fault planes, and various degrees of silicification, which are then followed by carbonation and pyritization; furthermore, fluoridation and clayization are also seen locally. The NNE-trending fold is characterized by the F401 and F403 faults, with a length of >3 km, a width of 5~20 m, and a fault displacement of 50~100 m. Additionally, the inner breccia is angular. The F201 fault is an NS-trending fold, and it mainly has a normal fault. There are relatively few EW-trending faults, such as F301 in the north of Jiadi Village and F302 in the south (Figure 2).
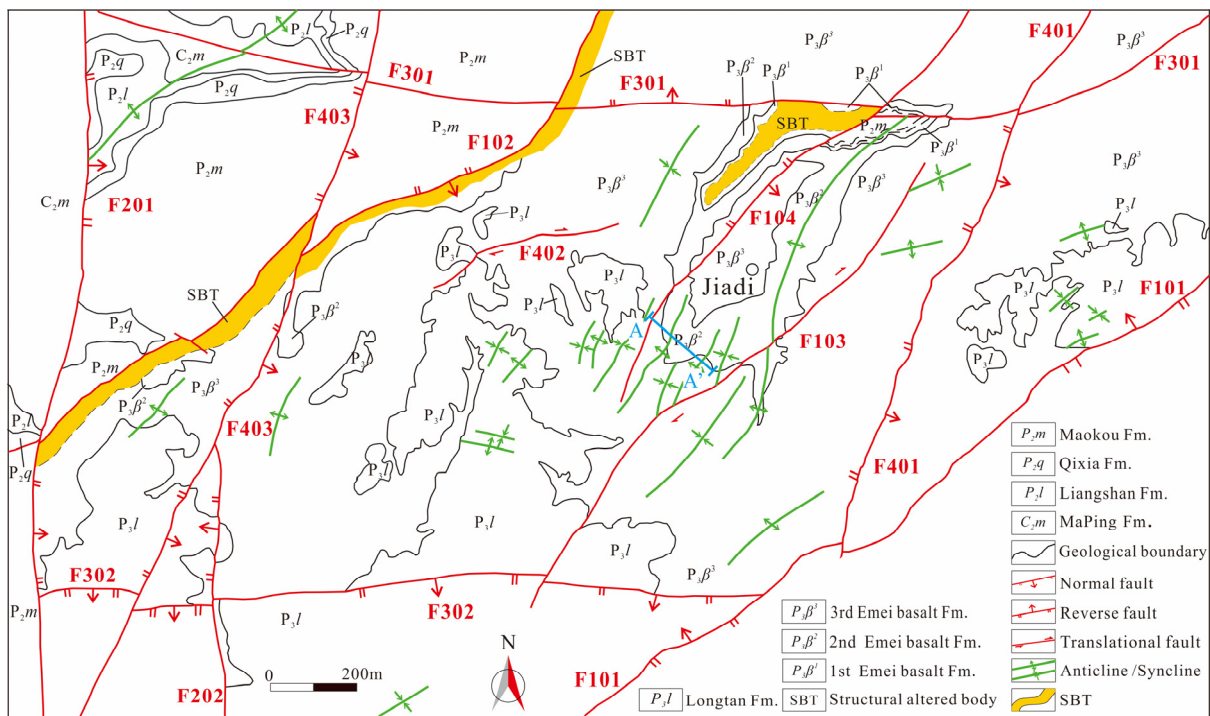
Figure 2. Geological map of the Jiadi gold deposit (modified from [27]).

The Jiadi deposit can be separated between upper and lower orebodies based on its spatial, structural, and stratigraphic properties (Figure 3). The lower layer is the No. 1 orebody at the unconformity interface between the limestone (P_2m) and Emeishan basalt ($P_3\beta^1$), which roughly coincides with the spatial distribution of structural alteration rock [28] and is dominated by tectonites, such as limestone, tuff, and basalt (Figure 3). Furthermore, the orebody is 150~300 m long and 110~260 m wide [13]. The upper layer is a No. 2 orebody in the second member of the Emeishan Basalt Formation ($P_3\beta^2$) basaltic breccia, which is the main ore-bearing horizon in the mining region and is 410 m long and 40~260 m wide. The orebody in the fold variation area is relatively thick, and the vertical distance between the two gold orebodies is 14~98 m [2,27].
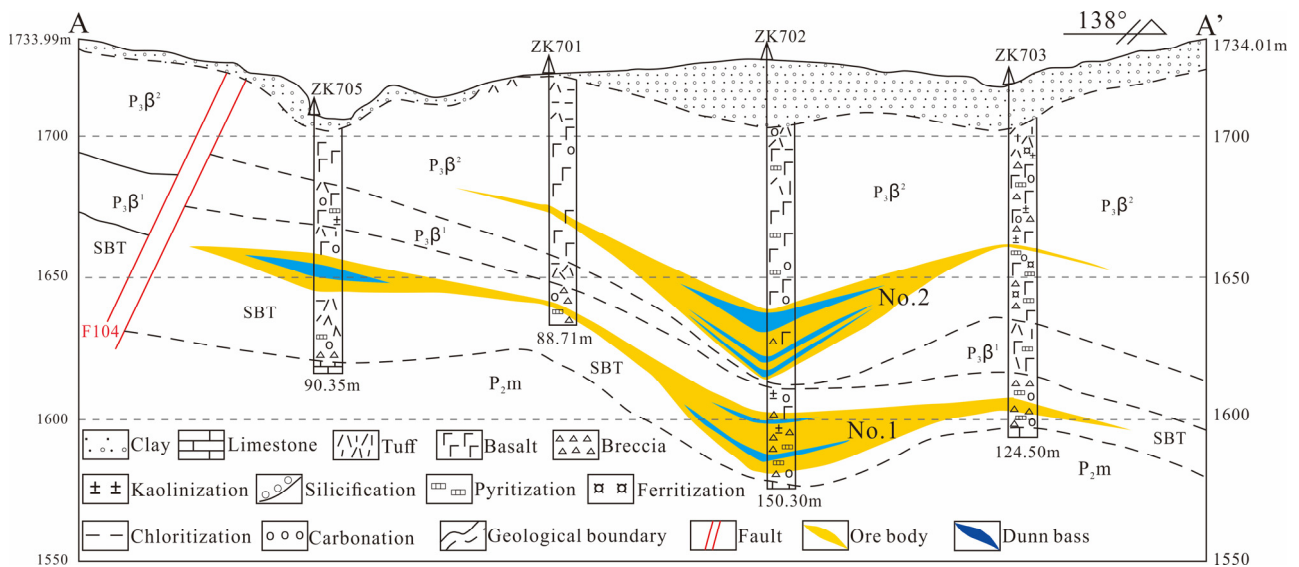

Figure 3. No. 7 exploratory profile of the Jiadi gold deposit (the positions of A and A' are shown in Figure 2) (modified from [29]).

The Jiadi gold deposit mainly includes structurally altered breccia-type ores (Figure 4b) and basaltic volcanic breccia-type ores (Figure 4a,c–f). The second member basalt group ($P^3\beta^2$) is a major rich orebody, and the rock of this layer is brittle and has a lesser hardness than the upper and lower massive basalt; it also demonstrates the different varieties of interlayer slip that occur during tectonic activity. The two most common metallic minerals are pyrite and arsenopyrite, followed by hematite, limonite, realgar, chalcopyrite, cinnabar, and stibnite. The non-metallic minerals are mainly quartz and carbonate minerals, followed by fluorite and clay minerals. Pyrite, arsenopyrite, and quartz, among others, have evident genetic links with gold mineralization [27].
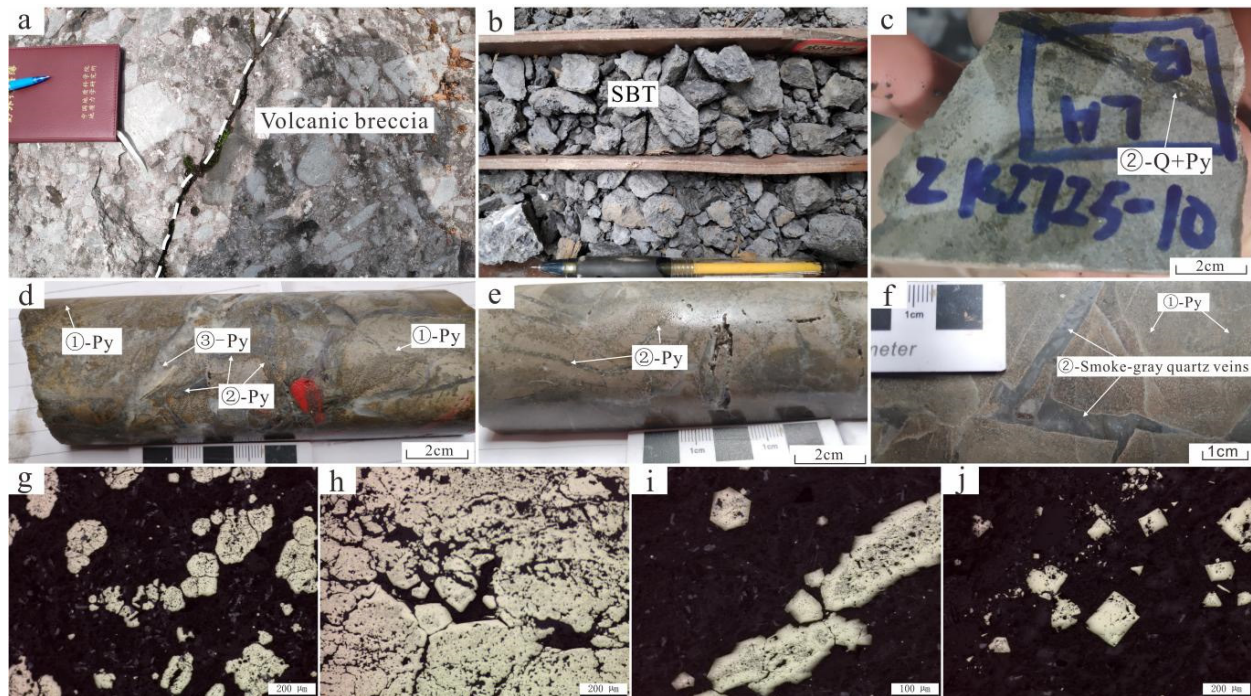
Figure 4. Identification of the metallogenic stages of the Jiadi gold deposit. (**a**) Altered volcanic breccia in the second member of the Emeishan basalt ($P_3\beta^2$); (**b**) drilling samples of the lower orebody; (**c**) quartz + pyrite veins of the smoky quartz stage; (**d**) pyrite + quartz veins of the smoky quartz stage are cut by the quartz veins of the sulfide stage; (**e**) the pyrite of the pyrite stage is metasomatized by the smoky quartz stage; (**f**) smoky quartz veins; (**g**) the framboidal pyrite formed in the pyrite stage; (**h**) the Au-bearing pyrite of the smoky quartz stage; (**i**) the pyrite veins of the smoky quartz stage; and (**j**) the euhedral–granular pyrite of the sulfide stage ((**g**–**j**) was taken under reflected light).

Based on the field observation and laboratory identification, with mineral assemblage and structural characteristics being accounted for, hydrothermal mineralization can be categorized into three stages: 1. The pyrite stage—framboidal pyrite is formed in the SBT, tuff, and basalt in the two orebodies, and a small amount of veined pyrite is accompanied by a small amount of arsenopyrite (Figure 4a) (which shows no obvious silicification and mineralization); 2. The smoky quartz stage—the main ore-forming stage characterized by smoky quartz veins is widely developed in two orebodies. Pyrite and other sulfides are found in the veins and often cut through the early pyrite veins (Figure 4h,i); 3. The sulfide stage—the sulfide is mainly developed in the upper orebody, and it reticulates the euhedral–semihedral pyrite (Figure 4j), realgar, and antimonite. It can also be seen in the quartz and carbonate veins, which also cut through the first two phases of pyrite veins [20].

4. Characteristics of Ore-Controlling Structure

In order to study the relationship between gold mineralization and tectonic activity, a field tectonic geological survey was carried out in the Jiadi gold deposit. The spatial

distribution characteristics of the folds, faults, joints, and striations were observed and measured. The plotting of structural elements was performed with Stereonet (Allmendinger 10.0), and the fault slip stress inversion was performed with Faultkin (Allmendinger 8.1). The structural events or elements described in this paper are represented by letters plus numbers to indicate the relative timing of the local deformation [30,31]. For example, D stands for deformation events; F for folds; S for faults, joints, and striations; and V for veins. As an example, V2 and S2 represent the veins and faults formed during the D2-deformation event.

4.1. Characteristics of Structural Deformation

The orebodies of the Jiadi deposit undulate and are distributed in the fold detachment space (Figure 3), and they are also close to the steep dipping fault structure. The lower orebody (No. 1) occurs in the interlayer fracture zone (SBT) between the limestone of the Permian Maokou Formation (P_2m) and the first member of Emeishan basalt ($P_3\beta^1$), which is similar to the Carlin-type gold deposit of the "Dachang Strata" (which is widely distributed in the Youjiang Basin [32]). The upper orebody is distributed in the basaltic volcanic breccia of the second member of the Emeishan basalt ($P_3\beta^2$). The basaltic primary ore is a special and primary ore-hosting type (such as the Damaidi gold deposit) of the Lianhuashan anticline [33].

The Jiadi gold deposit is located in the southeast flank of the Lianhuashan anticline in the area of strong structural deformations, and it has widely developed fold and fault structures. Its structural features are mainly NE-trending to NNE-trending, and it has an overall structure of "diamond lattice" composite structure characteristics. Two stages of fold structure were identified in the field investigation and observation: the first folding is NE-trending, and the second group is EW-trending. The characteristics of the fold indicate the existence of multi-stage tectonic activities.

(1)   Fold structure

Previous studies have suggested that the NE-trending Xinmachang anticline and Lianhuashan anticline were formed by NW-SE compression in the early Yanshanian [20,34]. The Xinmachang anticline is a regional structure with ambiguous features of hydrothermal activity. The rock strata on its northwest flank are relatively intact, and the folds and faults are mainly located in the southeast flank (Figure 1). The Lianhuashan anticline is the main ore-controlling structure of the Jiadi and Damaidi deposits. It is a secondary fold formed by the southeast flank of the Xinmachang anticline under late traction; it extends in a NE-SW-trending fashion and has a length of about 45 km and a width of 10~20 km [33].

The widely developed fold structure in the Jiadi deposit has a close spatial relationship with the distribution of the orebody. It is a monocline structure with a general dip of SE-trending regions and an undulating rock stratum with a dip angle of 0~25°. Field observation shows that the NE-trending fold is an anticlinorium that is relatively continuous and reworked by the later EW-trending fold (Figure 5b). The NEE-trending fold is consistent with the Lianhuashan anticline and is formed by NW compression at the same time (Figure 6b). Meanwhile, the basaltic breccia of the second member of the Emeishan Basalt and interlayer fracture zone (SBT) was formed. The EW-trending folds mainly crop out in the southwest of the Jiadi deposit, and the changes are not obvious, showing that they are reworked NE-trending folds (Figure 5a) (indicating that their formation time is later than the NE-trending main structure's).

(2)   Fault structure

Based on previous data, field investigation, and laboratory analysis, the faults can be divided into NS-trending normal faults, EW-trending normal faults, NE-trending reverse faults, and NNE strike-slip faults according to faults' strikes and properties.

Figure 5. Structural distribution characteristics of the Jiadi gold deposit. (**a**) The wide and gentle folds of the Jiadi anticline; (**b**) the NE-trending anticlinorium that was reworked by the EW-trending fold; (**c**) the NNE-trending faults; (**d**) the two stages of striations can be recognized on the fault plane; (**e**) the NE-trending faults; (**f**) the D1-deformation fault and fold are NS-trending; (**g**) the striations of the NE-trending fault surface; (**h**) the EW-trending faults; (**i**) the conjugated joint of D2-deformation; (**j**) the EW-trending faults; (**k**) the striations of the EW-trending faults; and (**l**) the conjugate joints of D1-deformation.

The NS-trending F201 fault is distributed in the west of the mining area, which is a regional deep large fault. It is a high-angle normal fault with a dip angle of more than 70°, a width of 50~300 m, a length of more than 3.5 km, and a fault displacement of more than 200 m. It is regarded as the preexisting fault structure in the area, and it was formed before the Permian [14]. Conjugate joints can be seen in tuff near the fault (Figure 5l), and the direction of the maximum primary stress is NE-trending (Figure 6k).

The EW-trending F301 and F302 faults are often obliquely cut by NE-trending and NNE-trending faults on the surface, which is a large-scale normal fault with a large-scale and long extension. It is the major structure that serves as a passageway for ore-forming in the area. The two stages of striations can be recognized as cutting through each other in a part of the fault plane (Figure 5d,h,k). Early striations on the fault plane indicate that the maximum principal stress direction is NE-trending (Figure 6e). Combined with the

previous data and the characteristics of the tectonic stress field, it is considered that the formation age of the fault is similar to that of the NS-trending fault.
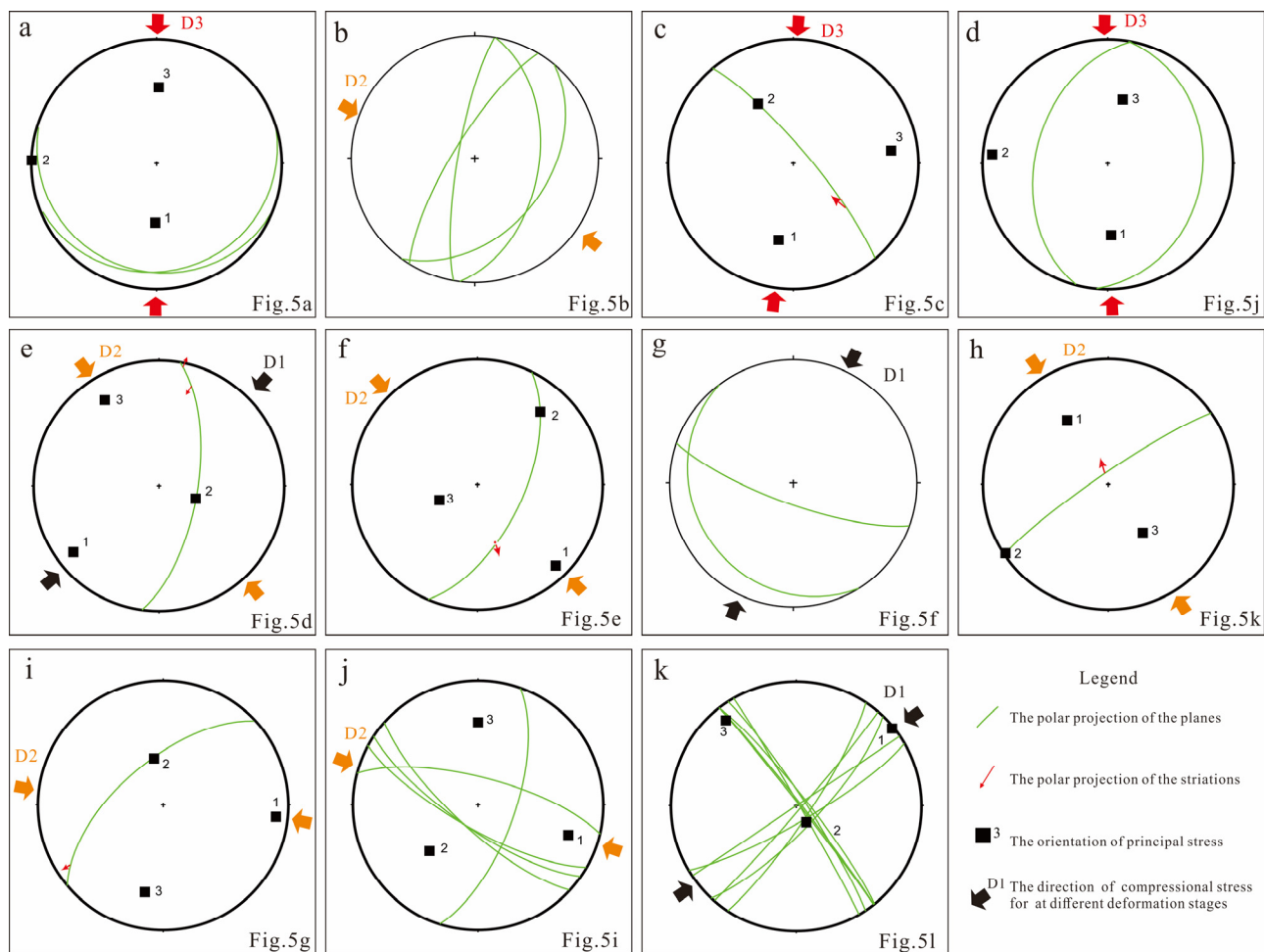
Figure 6. Recovery diagram of the tectonic deformation stress field. (**a**) The fold of D3-deformation; (**b**) the faults of D2-deformation; (**c**) the fault planes and striations of D3-deformation; (**d**) the faults of D3-deformation; (**e**) the inversion results of striations; (**f**) the normal fault of D2-deformation; (**g**) the fold of D1-deformation; (**h**) the high-angle fault of D2-deformation; (**i**) the fault and striation of D2-deformation; (**j**) the faults of D2-deformation; and (**k**) the conjugated joint of D1-deformation.

The NE-trending F101 and F102 faults mainly manifest as strike-slip reverse faults, which are cut by NNE-trending faults and are also cut through by the NS-trending and EW-trending faults. The maximum principal stress indicated by striation is NW-trending (Figures 5g and 6h). Both the NE-trending and stress field distributions indicate that they were formed in the same period as the main structure of the Lianhuashan anticline (Figures 5e and 6b). It has the multi-stage activity characteristics of first-compression and subsequent extension entireties, which provides channels for ore-forming fluid flow.

The NNE-trending F103, F401, F402, and F403 faults are the representative faults (Figure 5c,j). The direction of maximum compressive stress is nearly NS-trending, and the fault that cuts through the EW-trending and NE-trending faults early is widely developed in the region. This fault destroys the integrity of the fold belt for the Jiadi deposit, and it is a representative fault activity in the mineralization period [35].

4.2. Regional Tectonic Evolution

The aforementioned structural characteristics can be separated into four tectonic events, which are denoted as the D1 through D4 deformation periods, respectively, and are

based on superposition and a tangential relationship. The stress field characteristics of tectonic events and their relationship are described below, including the relationship between tectonic-superimposed deformations, tectonic activations, and gold mineralization.

The D1-deformation event was the earliest deformation period observed in the field, and it is a tectonic event characterized by fault (S1) (Figures 5f and 6g). The faults are NS-trending and EW-trending, and most of the faults are steep (68~88°). They were formed earlier than the formation age of the Lianhuashan anticlinorium, and the maximum principal stress direction is NE-trending (Figure 6g). Previous studies believed that the Shizong–Mile fault started to be active since the Devonian and that the NS-trending and EW-trending fault structures in the study were derived structures. The Indosinian area was slowly uplifted to form a sedimentary discontinuity at the top of the Maokou Formation, which was then overlain by the Emeishan basalt. The fault distribution is mainly controlled by boundary faults.

The D2-deformation event included NE-trending folds (F2) and NE-trending faults (S2) that constitute the basic structural framework of the Lianhuashan anticline. The F2 fold hinge in Jiadi is NE-trending, which is consistent with the strike of the Lianhuashan anticline and is the main tectonic age of the regional interformational sliding (Figure 5a). According to the fold (Figure 6b) and fault (Figure 6e,f,h,i) inversion tectonic stress field, the Lianhuashan area is mainly characterized by the reverse movement of the Shizong–Mile fault, which formed the NE-trending Lianhuashan anticline (F2) and the NE-trending fault structure (S2), thus corresponding to the regional compression stress of NW-SE in the early Yanshanian [14].

The D3-deformation event was manifested as EW-trending folds (F3) and NNE-trending faults (S3) (Figure 5a), and it was based on the crosscutting relationship and property difference between S2 and S3 (this period is regarded as the smoky quartz stage of the regional stress transformation). Fold structures are sporadically exposed at the southwest of the Jiadi (Figure 2), the hinge is dominated by the EW-trending faults, and the maximum displacement direction is approximately NS-trending (Figure 6a,d). The S3 fault is mainly characterized by a strike-slip-normal fault, which is consistent with the extensive NE-trending structural belts (such as the Huijiabao and Getang anticlines) and was developed in the southwestern Guizhou region in the late Yanshanian period. Meanwhile, the axial variation of the Lianhuashan anticline formed a reversed "S" NNE-trending fault structure (S3), which is bounded by the NE-trending Xinmachang anticline. The northwest flank has relatively complete rock formations, and the southeast flank has relatively developed faults, folds, and interlayer-fractured alteration zones. This period was the main period of tectonic transformation and gold mineralization [35].

The D4-deformation event saw faults that were rarely developed in the later mineralization period in the mining area; they are mainly micro-structures that were formed by the intraplate activities in the Himalayan period. Furthermore, basin-controlling faults were also formed, which manifested as the activation and derivation of early structures. In addition, the fault activities caused damage and dislocation to the orebodies and early structural features.
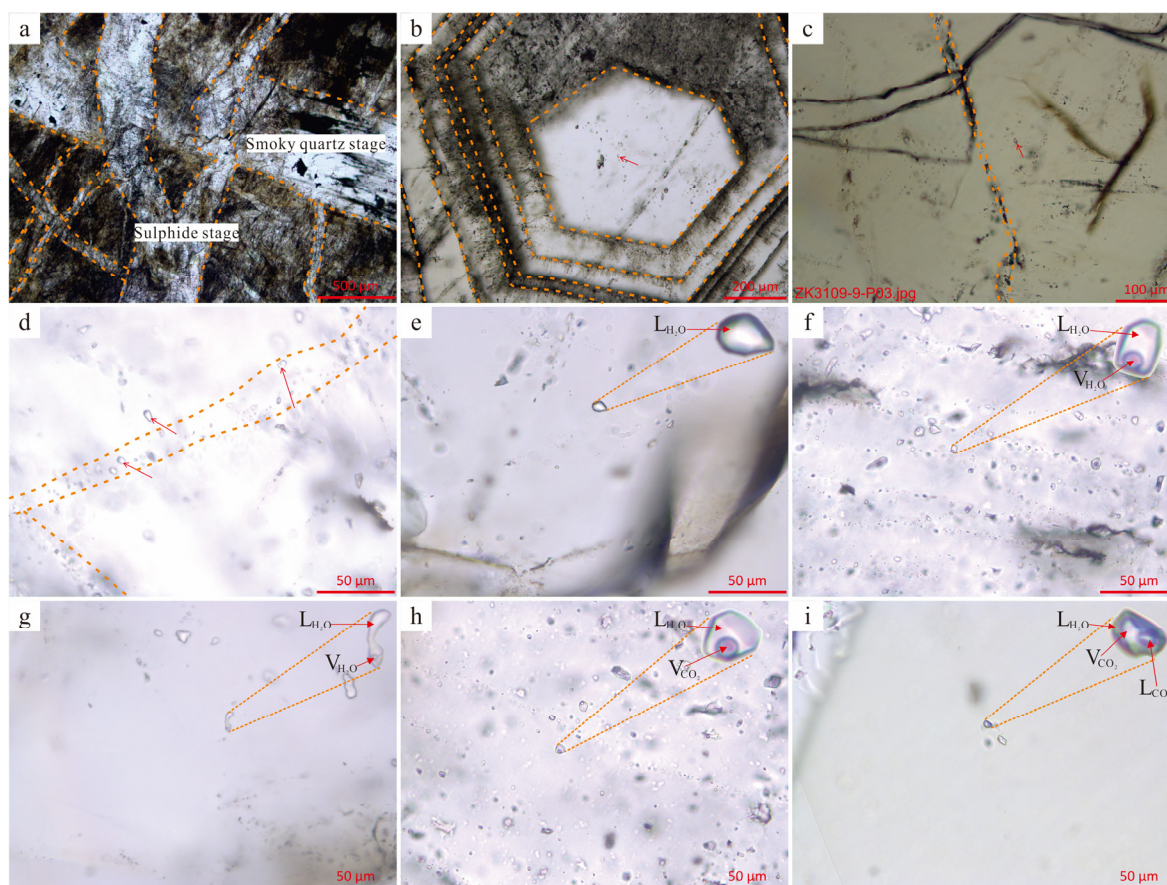
5. Fluid Inclusion

5.1. Sample Collection

The chemical composition and physicochemical properties of ore-forming fluids can be obtained by microthermometry and a laser Raman spectroscopy (LSR) analysis of the fluid inclusions of quartz and calcite [35–39], thereby indicating the composition, property, source, and evolution of ore-forming fluids [40]. In this paper, 25 samples from the No. 9 borehole of Exploration Line 31 were collected, mainly from the volcanic breccia ore of the Emeishan Basalt Formation ($P_3\beta^2$), and this was followed by the structural alteration body (SBT) of the lower orebody and carbonaceous tuffite of the third member of the Emeishan Basalt Formation ($P_3\beta^3$).

5.2. Fluid Inclusion Petrography

Based on the vein-cutting relationship observed at room temperature (Figure 7), the fluid inclusion assemblage and the phase state were conducted at the fluid inclusion at room temperature (20 °C), and the test results of the fluid inclusion LSR were combined. The fluid inclusions of the gold deposits are divided into $NaCl-H_2O$ (A) and $CO_2-NaCl-H_2O$ (B). The primary and pseudosecondary inclusions dominate (Figure 4b,d), with sporadic secondary inclusions (Figure 7c).

Figure 7. The petrographic characteristics of the fluid inclusions in the Jiadi gold deposit. (**a**) The smoky quartz veins were cut by sulfide veins; (**b**) the zonal structure of quartz; (**c**) the secondary inclusions in quartz; (**d**) the fluid inclusion assemblage; (**e**) the A1-type inclusion; (**f**) the A2-type inclusion; (**g**) the "neck-down" inclusion; (**h**) the B1-type inclusion; and (**i**) the B2-type inclusion.

(1) $NaCl-H_2O$ type inclusions (A)

Such inclusions are composed of NaCl and H_2O, which can be divided into single-phase $NaCl-H_2O$ (A1) and two-phase $NaCl-H_2O$ (A2), according to the phase state at ambient temperature (the latter of which is relatively common). Inclusions were found in the crystals of the quartz and calcite minerals, whereby most of them were elliptic and linear, as well as in small groups. Occasionally, the "neck-down" phenomenon (Figure 7g) was observed, and these minerals were 3~12 μm in size (some more than 12 μm) with a gas–volume ratio of 2%~9%.

(2) $CO_2-NaCl-H_2O$ type inclusions (B)

These inclusions are characterized by CO_2 enrichment and can be divided into two-phase $CO_2-NaCl-H_2O$ (B1) and three-phase $CO_2-NaCl-H_2O$ (B2) (Figure 7i) (the former of which is relatively common). They mainly occur in quartz and are mostly scattered, clumpy, and irregular-banded (Figure 7d). Only a small amount is found in calcite. They

are often accompanied by the NaCl-H$_2$O type with 4~14 μm, some of which can reach more than 20 μm, with a gas–volume ratio of 4%~13%.

5.3. Microthermometry of the Fluid Inclusions

The fluid inclusions in the samples were determined by homogenization and freezing. When the homogenization temperature (T_h) was measured, the early heating rate was 15.0 °C/min. When it approached the phase transition, the heating rate decreased to 1.0 °C/min and 0.5 °C/min. In the freezing point measurement, it rapidly decreased at a rate of 10 °C/min and then gradually increased after it reached −60 °C. The heating rate decreased from 10 °C/min at the beginning to 2 °C/min. It then decreased to 0.2 °C/min near the phase transition. These phase transitions of the inclusion were observed and recorded (Tables 1 and 2). For detailed instrument parameters and experimental procedures, please refer to the references [1,38].

The results of microthermometry show that A-type inclusions are developed in quartz and calcite, and they are formed at different stages of hydrothermal mineralization. The eutectic temperature of the inclusions was between −26.6 °C and ~−20.3 °C; the freezing point temperature was between −4.8 °C and ~−0.5 °C, and the homogenization temperature (T_h) was between 162 °C and ~231 °C (Figure 8a). The salinity Wt (NaCleq) ranged from 0.9% to ~7.6% (Figure 8b). The homogenization temperature (T_h) of the pyrite stage was from 211 °C to 231 °C, the homogenization temperature (T_h) from 182 °C to 218 °C, and the homogenization temperature (T_h) of the sulfide stage was generally lower than 183 °C. The fluid salinity can be calculated by the salinity-freezing point formula of the NaCl-H$_2$O system (where Wt (NaCleq) (%) is salinity and T_m (°C) is freezing point temperature): Wt (NaCleq) = $0.00 + 1.78T_m - 0.0442T_m^2 + 0.000557T_m^3$ (only applicable to the two-phase NaCl-H$_2$O inclusions with a salinity between 0%~23.3%). The density was estimated by using the homogenization temperature (T_h) and salinity value in the pressure–temperature–concentration–density relationship of the NaCl-H$_2$O system [41].

The B-type inclusions in the Jiadi gold deposit were mainly distributed in the pyrite stage and the smoky quartz stage. The results of the temperature measurement showed that the eutectic melting temperature was between −59.0 °C and ~−56.0 °C; the melting temperature of clathrate was between 4.0 °C and ~9.8 °C; the homogenization temperature was between 179.0 °C and ~229.0 °C, and the salinity Wt (NaCleq) was between 1.2% and ~7.2%. The fluid salinity can be obtained by the formula Wt (NaCleq) = $15.52022 - 1.02342T_{am} - 0.05286T_{am}^2$ (Roedder, 1984). The saltwater density can be obtained from the above values of homogenization temperature and the salinity in the parameter table of the CO$_2$-NaCl-H$_2$O system [42].
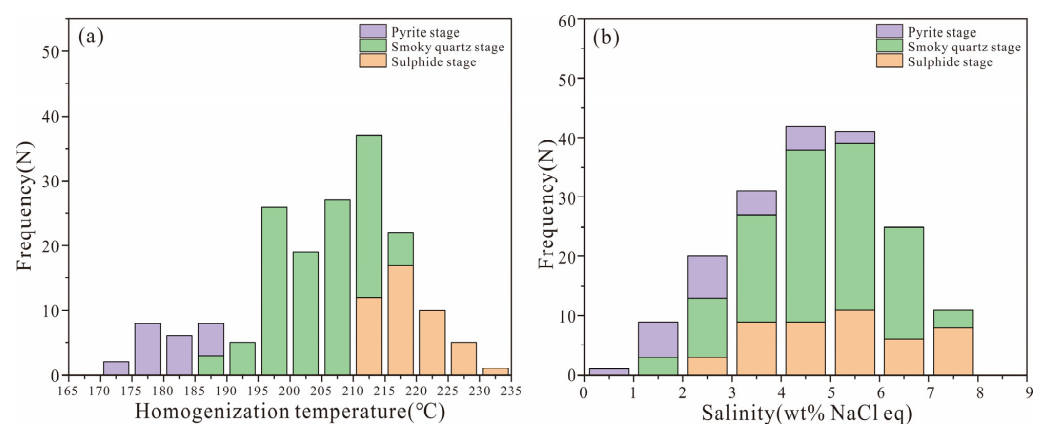
Figure 8. The homogenization temperature/salinity and frequency histogram of the fluid inclusions. (**a**) The homogenization temperature frequency histogram of the fluid inclusions; (**b**) the salinity frequency histogram of the fluid inclusions.

Table 1. The Parameters of two-phase NaCl-H$_2$O fluid inclusions.

Number	Strata and Host Minerals	Type	Number of Test	Eutectic Melting/°C Range	Average	Homogenization/°C Range	Average	Freezing/°C Range	Average	Salinity/wt% (NaCl eq) Range	Average	Density/(g/cm^3) Range	Average	Stage of Mineralization
ZK3109-1	SBT (Cal)	A2	10	−23.8~−20.3	−22.05	231~206	215	−2.3~−4.8	−3.8	7.6~3.9	6.1	0.883~0.903	0.893	Pyrite
ZK3109-2	P$_3\beta^2$ (Cal)	A2	7	−24~−21.1	−22.55	218~199	208.3	−1.2~−4.7	−3.1	7.4~2.1	5.0	0.878~0.909	0.894	Pyrite
ZK3109-4	P$_3\beta^2$ (Q)	A2	7	−21.6~−20.4	−21	225~199	209.7	−1.7~−4.5	−3.3	7.2~2.9	5.4	0.877~0.915	0.896	Pyrite
ZK3109-5	P$_3\beta^2$ (Q)	A2	7	−24.6~−21.4	−23	235~198	213.1	−1.5~−4.0	−2.9	6.4~2.6	4.8	0.867~0.907	0.887	Pyrite
ZK3109-7	P$_3\beta^2$ (Q)	A2	7	−22.8~−21.1	−21.95	225~198	209.1	−1.9~−4.2	−2.9	6.7~3.2	4.8	0.868~0.907	0.888	Pyrite
ZK3109-8	P$_3\beta^2$ (Q)	A2	9	−23.2~−20.7	−21.95	223~195	212.4	−1.8~−4.3	−3.0	6.9~3.1	5.0	0.871~0.908	0.890	Pyrite
			8	−21.8~−20.5	−21.15	196~177	187.0	−0.8~−3.0	−1.9	5.0~1.4	3.2	0.882~0.926	0.904	Smoky quartz
ZK3109-10	P$_3\beta^2$ (Q)	A2	9	−24.3~−21.4	−22.85	223~198	211.9	−1.7~−4.7	−2.9	7.4~2.9	4.7	0.872~0.909	0.891	Pyrite
ZK2725-4	P$_3\beta^2$ (Q)	A2	9	−22.7~−20.4	−21.55	222~188	205.7	−1.5~−3.5	−2.5	5.7~2.6	4.2	0.860~0.919	0.890	Smoky quartz
ZK2725-5	P$_3\beta^2$ (Q)	A2	5	−21.9~−20.6	−21.25	218~195	207	−1.8~−3.6	−2.6	5.9~3.1	4.4	0.882~0.897	0.890	Pyrite
ZK2725-9	P$_3\beta^2$ (Q)	A2	7	−23.1~−21.6	−22.35	215~193	206.9	−1.9~−3.2	−2.7	5.3~3.2	4.4	0.875~0.912	0.894	Pyrite
ZK2725-12	P$_3\beta^2$ (Q)	A2	9	−23.7~−21.1	−22.4	217~185	20.1	−2.1~−3.6	−2.9	5.9~3.5	4.6	0.872~0.910	0.891	Smoky quartz
ZK2725-13	P$_3\beta^2$ (Q)	A2	7	−26.6~−21	−23.8	213~195	204.8	−2.2~−3.6	−2.8	5.9~3.7	4.6	0.884~0.970	0.896	Pyrite
ZK2725-15	P$_3\beta^2$ (Q)	A2	8	−24.2~−21.9	−23.05	215~196	205.5	−1.7~−3.7	−2.6	6.0~2.9	4.3	0.870~0.908	0.889	Pyrite
ZK3125-1	P$_3\beta^2$ (Q)	A2	9	−23.6~−21.7	−22.65	180~162	170.8	−0.5~−1.6	−1.0	2.7~0.9	1.8	0.905~0.930	0.918	Sulfide
ZK4204-1	P$_3\beta^2$ (Q)	A2	7	−24.4~−21.8	−23.1	213~176	197.3	−1.5~3.2	−2.3	5.3~2.6	3.8	0.871~0.931	0.901	Sulfide
ZK4204-2	P$_3\beta^2$ (Q)	A2	7	−25.1~−20.8	−22.95	223~198	208.1	−2.5~−4.7	−3.7	7.4~4.2	5.9	0.882~0.913	0.898	Pyrite

Table 2. The Parameters of two-phase CO$_2$-NaCl-H$_2$O fluid inclusions.

| Number	Strata and Host Minerals	Type	Number of Test	Eutectic Melting/°C Range	Average	Clathrate Melting/°C Range	Average	Homogenization/°C Range	Average	Freezing/°C Range	Average	Salinity/wt% (NaCl eq) Range	Average	Density/(g/cm^3) Range	Average	Stage of Mineralization
ZK3109-3	P$_3\beta^2$ (Q)	B1	7	−59~−56	57.5	4.0~9.8	6.9	229~197	209.8	−1.0~−4.7	−3.3	6.4~1.7	4.7	0.875~0.961	0.918	Pyrite
ZK3109-6	P$_3\beta^2$ (Q)	B1	7	−58.1~57	57.6	6.8~8.1	7.5	224~198	210.7	−1.7~−4.5	−3.2	7.2~2.9	5.2	0.845~0.958	0.902	Pyrite
ZK3109-9	P$_3\beta^2$ (Q)	B1	10	−58.3~−56.7	57.5	5.3~8.7	7.0	227~197	211.3	−1.5~−4.0	−3.0	6.4~2.6	4.9	0.852~0.928	0.890	Pyrite
	P$_3\beta^2$ (Q)	B1	8	−57.2~−56.7	57.0	5.3~8.4	6.9	201~179	188.1	−0.7~−3.0	−1.7	5.0~1.2	2.9	0.831~0.930	0.881	Smoky quartz
ZK3109-12	P$_3\beta^2$ (Q)	B1	9	−58.6~−57.3	58.0	7.4~9.3	6.9	220~179	198.6	−1.8~−4.1	−2.9	6.6~3.1	4.8	0.862~0.918	0.890	Pyrite
ZK2725-14	P$_3\beta^2$ (Q)	B1	7	−58.8~−57.1	58.0	7.0~9.4	8.2	224~195	210.3	−2.1~−4.1	−3.2	6.6~3.5	5.2	0.875~0.960	0.918	Pyrite

Host minerals: Q—Quartz; Cal—Calcite. Sampling horizon: P$_3\beta^2$—The upper volcanic breccia ore body; SBT—the lower structural alteration ore body. The inclusion types: A2—the two-phase NaCl-H$_2$O; B1—the two-phase CO$_2$-NaCl-H$_2$O.

5.4. Laser Raman Spectroscopy (LSR) Analysis

LSR was conducted at the Beijing Research Institute of Uranium Geology, CNNC. For specific instrument parameters and analytical methods, please refer to the literature [43]. Through using the LSR method for the fluid inclusions formed at different stages, the results show that the A-type inclusions were more dominant generally, followed by the B-type—in which there existed an especially small amount of reducing gas components.

The composition of the inclusions in the pyrite stage was relatively simple: mainly composed of H_2O and NaCl, followed by CO_2. The composition of the inclusion in the smoky quartz stage was relatively complex, and it contains gas phase components such as CO_2, CH_4, SO_2, H_2S, and N_2 (Figures 7d and 9c). In the sulfide phase, the fluid inclusions were small and numerous, and the Raman spectra showed that the gas-phase component was mainly composed of H_2O. By comparing the results of laser Raman analysis with the petrographic characteristics of the fluid inclusions and microthermometry, it was found that the fluid in the pyrite stage is more CO_2 rich, while the fluid in the smoky quartz stage had more types of reducing gases (and the CO_2 decreased along with the fluid evolution) [44].
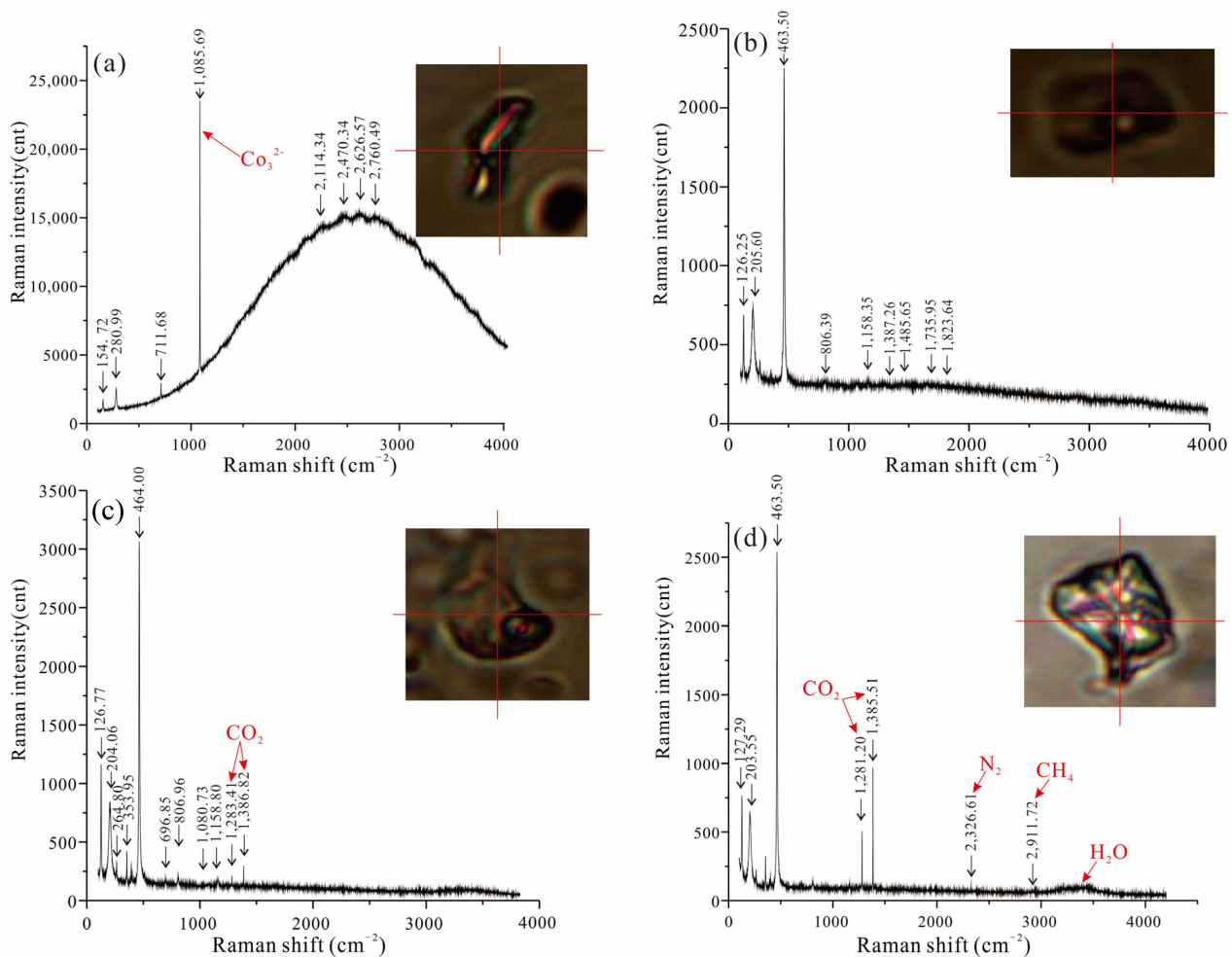
Figure 9. The LSR characteristics of the fluid inclusions in the Jiadi gold deposit. (**a**) The A-type gas–liquid two-phase inclusions in the pyrite stage; (**b**) the A-type gas–liquid two-phase inclusions containing a small amount of gas-phase compositions in the smoky quartz stage; (**c**) the three-phase inclusions containing a small amount of CO_2 in the smoky quartz stage; and (**d**) the two-phase inclusions containing CO_2, CH_4, and N_2 in the sulfide stage.

6. Stable Isotope Geochemistry

6.1. Sample Collection and Analysis Method

Based on the division of the metallogenic stages, this paper selects high-purity quartz and pyrite in different metallogenic stages, exploits an isotope mass spectrometer (MAT 253) to carry out analysis, discusses the source of metallogenic materials and the regularity of fluid evolution, as well as reduces the metallogenic process of the Jiadi gold deposit. Stable isotope analysis was completed at the Beijing Research Institute of Uranium Geology, CNNC. Please refer to the literature for specific analysis techniques and instrument specifications [45].

6.2. Carbon and Sulfur (C-S) Isotope Geochemistry

The amount of CO_2 in the ore-forming fluid was significantly higher than that of other gases in every evolution stage. CO_2 is the primary carrier of carbon compositions in a fluid system, and the influence of other carbon-containing gases on the analysis results can be disregarded. Therefore, by measuring the $\delta^{13}C$ value in the CO_2 of quartz fluid inclusions, we can approximately represent the carbon isotopic composition of the entire fluid system. The values of the carbon isotopes of the six quartz fluid inclusions in the hydrothermal metallogenic period of the Jiadi gold deposit ranged from −5.5‰ to ~−7.2‰ (Figure 10b), with an average of −6.35‰. These values demonstrated relatively consistent and concentrated distribution characteristics, indicating that the carbon isotopes in each metallogenic stage have relatively consistent sources. Through comparing the carbon isotopic composition of the Jiadi gold deposit with the carbon reservoir, when combined with the prediction of regional concealed granite, it was considered that the source of the carbon was mainly from a deep source, and it is most likely the product of crustal magmatic differentiation.
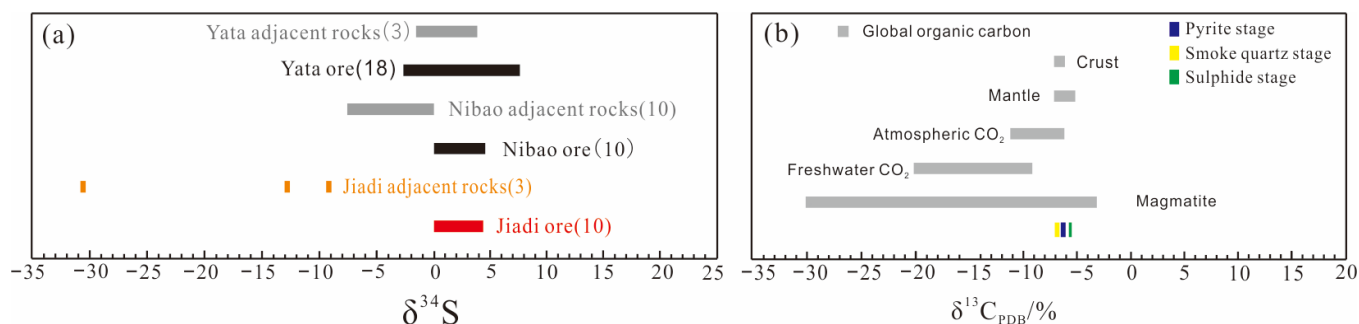
Figure 10. The $\delta^{34}S$ and $\delta^{13}C_{PDB}$ diagram isotope composition of the Jiadi golden deposit [1]. (**a**) The sulfur isotope composition of the deposit; (**b**) the carbon isotope composition of the deposit.

The sulfur isotope analysis object of the Jiadi gold deposit was the single pyrite mineral. The results show that the $\delta^{34}S$ values of the three adjacent rocks ($P_3\beta$) have values of −30.7‰, −12.8‰, and −9‰ and that the isotopic composition is extremely dispersed. The $\delta^{34}S$ values of the 10 pyrites associated with mineralization ranged from 0.5 to ~4.5‰, with an average of 2.5‰ (Figure 10a). The mineralized samples have a relatively evident indicative effect, suggesting that the sulfur in the ore-forming fluid of the Jiadi gold deposit should be mainly from a deep source. The sulfur isotopic composition of the pyrite selected from the surrounding rock strata is characterized by a large negative value range, which is clearly different from the sulfur isotopic composition in the concentrated ore-forming fluid. The data distribution of this pyrite is relatively similar to that of the reduced sulfur in the sedimentary strata [46].

6.3. Hydrogen and Oxygen (H-O) Isotopes Geochemistry

H-O isotope testing was carried out on six quartz samples from the Jiadi deposits, and the results showed that the δD_{v-smow}/‰ data varied from −90‰ to −72.8‰, with an

average of −81.4‰. Furthermore, the $\delta^{18}O_{v\text{-}smow}$/‰ data ranged from 19.3‰ to 21.9‰, with an average of 20.6‰. According to the oxygen isotope equilibrium fractionation equation between quartz and water $1000\ln\alpha_{Quartz\text{-}water} = 3.38 \times 10^6/T^2 - 3.40$ [47], the obtained $\delta^{18}O_{H2O}$ data varied from 0.8 to ~3.2‰, with an average of 2.0‰. According to the assumption regarding the inclusion of quartz minerals, this value represents the isotopic composition of the ore-forming fluid [6,48]. The data points show that the variation range of the isotopic composition is concentrated, and the data points are located in the left region of magmatic fluid, indicating that the ore-forming fluid has the characteristics of metamorphism/magmatic fluid and local meteoric water.

Under different temperature conditions, water/rock ratios (W/R), and initial fluids (assuming that the ore-forming fluid metasomatizes the limestone), we depicted the evolution curve of the hydrogen and oxygen isotopic composition of the fluid in a water–rock exchange reaction [49]. According to the microthermometry results of the fluid inclusions, the homogenization temperatures of the pyrite stage, smoky quartz stage, and sulfide stage of the ore formation were 220 °C, 200 °C, and 180 °C, respectively (these also correspond to the gray, red, and blue lines, respectively, in Figure 11). The results show that the data points are located in the area of low W/R ratios of meteoric water. This indicates that magma may provide a source of heat in the pyrite stage of mineralization and that a small amount of deep circulating atmospheric water rises into ore-forming fluid after deep high-temperature heating.
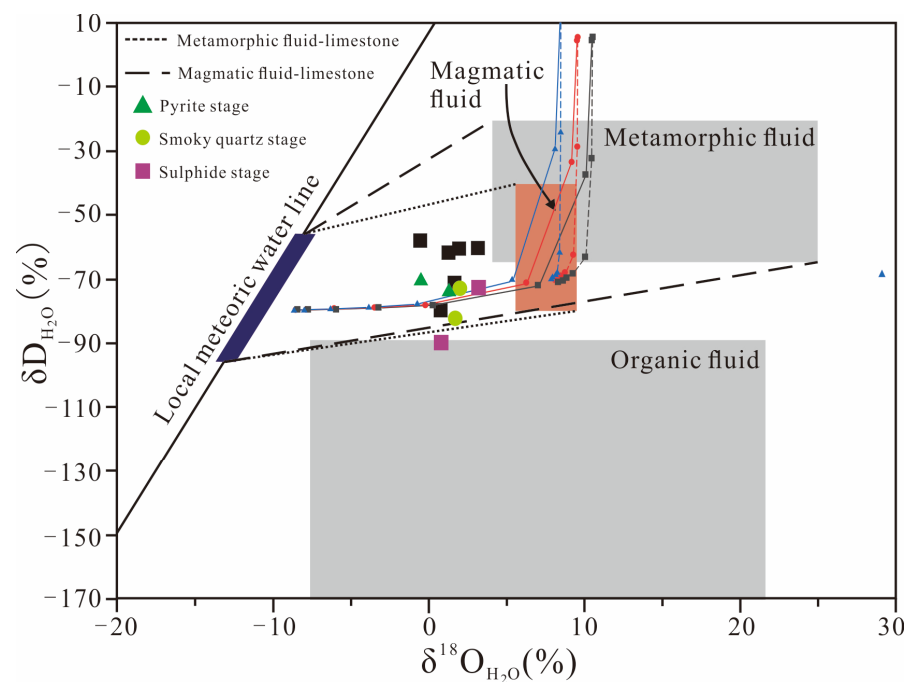
Figure 11. The δD vs. $\delta^{18}O_{H2O}$ diagram of the hydrothermal quartz in the Jiadi deposit [50–52].

7. Discussion

7.1. Ore-Forming Fluid and Gold Mineralization

The results show that the fluid inclusions in the Jiadi gold deposit can be divided into A-type and B-type and that they contain a small amount of gas-phase compositions, such as CH_4, CO, H_2S, and N_2. The homogenization temperature (T_h) of the fluid inclusions was between 162 and ~235 °C, and the salinity Wt (NaCleq) was between 0.9% and ~7.6%. The eutectic melting temperature of the A-type inclusions was slightly lower than −20.8 °C, indicating that, in addition to NaCl, the A-type inclusions also contained a low content of components with a low-eutectic temperature with H_2O [42]. The eutectic melting temperature of the CO_2-containing fluid inclusion was lower than the triple-point temperature of pure CO_2 (−56.6 °C), indicating the presence of a minor amount of CH_4 or N_2 (which is

consistent with the laser Raman spectral data). In the pyrite stage of mineralization, fluid inclusions have the characteristics of high temperature and high salinity and have more reducing gases, which have the characteristics of a deep source. The fluid temperature and salinity continue to decrease with the evolution of ore-forming fluid, and the CO_2 and other gases boil and escape during fluid mixing and decompression [41].

The study of the H-O isotopes of the ore-forming fluid of Carlin-type gold deposits in Southwest Guizhou shows that the variation range of the H-O isotopes of ore-forming fluid is concentrated, which is located between magmatic water and meteoric water. The H-O isotope exchange curve shows that the ore-forming fluid is dominated by magmatic water in the pyrite stage and superimposed with deep circulating atmospheric water in the sulfide stage, which occurs under the condition of low W/R ratios. Furthermore, the influence of temperature on the variation of H-O isotope composition was limited, indicating that the time for gold mineralization was relatively concentrated. Meanwhile, the carbon isotope of the quartz and sulfur isotopes of pyrite showed that the metallogenic materials have the characteristics of a deep source, which is consistent with the evolution of fluid inclusions [53–56].

7.2. Tectonic Activity and Gold Mineralization

The crust is characterized by a gentle uplift during the Indosinian stage rather than overt fold deformation. The rapid and large-scale uplift of the crust and the domal uplift before the eruption of the Emeishan basalt were the principal tectonic background, forming regional NS-trending and EW-trending structures. The Emeishan mantle plume provides a certain heat source and fluid source for regional mineralization. The principal fault of the deep basement is the fluid channel of the deep hydrothermal and meteoric water, and the widely developed interlayer slip surface in the region is the lateral migration channel of metallogenic fluid [57,58].

The early Yanshanian was dominated by NW compression, forming NE-trending folds and fault (D2) in the Lianhuashan anticline, resulting in early tectonic activation and interlayer detachment; this provided the basic tectonic framework of this region's tectonic areas. It was the strongest tectonic movement in Southwest Guizhou since the Paleozoic. In addition, the Yanshanian magmatic rock intrusion was also formed in this region [14]. In the late Yanshanian period, with the acceleration of the northward movement of the Indian plate, a regional tectonic stress field compressed from SSW to NNE and was formed in China [36]. Large-angle obliques span the structural superposition that occurred in Central Guizhou and its surrounding regions. The nearly NE-trending fold in the late Yanshanian period underwent a leftward shear to a form reversed "S"-shaped superimposed fold (D3), while the early NE-trending fault activity was characterized by a leftward shear again, and the nearly NS-trending fault was characterized by a tensional normal fault. Under the background of regional extensional structures and magmatic upwellings, the fluid migrated upward along the faults of the basement fault and migrated laterally on the interlayer sliding surface to precipitate mineralization [35].

7.3. Structure–Fluid Coupling Mineralization

Before the eruption of the Emeishan basalt in the Indosinian period, the crust was uplifted and domed, forming regional EW-trending tensional deep fault structures. The strong NW compression in the early Yanshanian essentially established the NE-trending regional tectonic pattern, and the interlayer detachment layer was formed at the interface with different energy and dryness [59,60]. Under the background of regional tectonic transformation in the late Yanshanian, the ore-forming fluid related to the deep magmatic evolution upflowed along the EW-trending faults. The ore-bearing overpressure fluid was rich in CH_4, N_2, CO_2, and H_2O, and it also had a high W/R ratio exchange reaction in the fault zone and interlayer fracture zone. Furthermore, CO_2 escaped when mixed with atmospheric water, which is precipitated and mineralized in the tectonic detachment surface between the Maokou Formation (P_2m) and Emeishan basalt, as well as in the basaltic breccia

of the second member of the Emeishan basalt ($P_3\beta^2$). The tuff of the Emeishan Formation and clay rock of the Longtan Formation showed a stable distribution at the anticline flank, which makes the ore-forming fluid migrate laterally along the low-pressure region of horizontal breccia. Furthermore, the water–rock metasomatism occurred simultaneously, resulting in the precipitation of gold with pyrite and arsenopyrite [61,62].

8. Conclusions

(1) The Jiadi gold deposit is situated in the strong deformation area of the southeast flank of the Lianhuashan anticline. The four stages of structural deformation closely related to mineralization were identified by structural analysis. The NE-trending Lianhuashan anticline was formed by NW compression in the early Yanshanian period, and the early structure was activated in the late Yanshanian period. It is believed that the structural alteration caused by the D3-deformation event served as the primary backdrop for gold mineralization;

(2) The fluid inclusions were divided into A-types and B-types, with the pyrite stage of mineralization being dominated by CO_2-rich inclusions and the smoky quartz stage having a significant amount of gas-phase compositions, such as CO_2, CH_4, and N_2. The fluid components in the sulfide stage of mineralization were relatively simple, and the temperature and salinity gradually decreased in the process of fluid evolution. The H-O isotope showed that the initial ore-forming fluid was primarily magmatic water, which is mixed with meteoric water in the sulfide stage; furthermore, the C-S isotope showed that the metallogenic materials originate primarily from deep sources;

(3) The early Yanshanian compressional deformation of the Jiadi gold deposit resulted in magmatic upwelling and formation dehydration, which produced a significant amount of CO_2-rich and low-salinity fluids. In the late Yanshanian period, the deep fluid migrated up the fault to the interlayer fracture zone. Moreover, there was also the addition and mixing of meteoric water with the magmatic–hydrothermal solution, which led to a change in the geochemical environment, thus resulting in the quick precipitation of metallogenic materials.

Author Contributions: W.Z. and J.P. put forward the research direction; Z.M. and Z.Z. analyzed the data and wrote the paper; H.H. treated samples and performed experiments; G.H. searched the literature. Moreover, thanks are given to journal reviewers and editors for their constructive comments on the manuscript. All authors have read and agreed to the published version of the manuscript.

Data Availability Statement: Data is contained within the article.

Conflicts of Interest: The authors declare no conflict of interest.

References

1. Xie, X.Y.; Feng, D.S.; Chen, M.H.; Guo, S.X.; Kuang, S.D.; Chen, H.S. Fluid inclusion and stable isotope geochemistry study of the Nibao gold deposit, Guizhou and insights into ore genesis. *Acta Petrol. Sin.* **2016**, *32*, 3360–3376. (In Chinese)
2. Li, X.; Zhou, Z.G.; Zhang, M.F.; Jin, Y.J. Geological characteristics and ore-controlling structure of jiadi gold deposit in Lianhuashan area, Guizhou Province. *Acta Mineral. Sin.* **2015**, *35*, 223–224. (In Chinese) [CrossRef]
3. Liu, J.Z.; Deng, Y.M.; Liu, C.Q.; Zhang, X.C.; Xia, Y. Metallogenic conditions and model of the superlarge Shuiyindong stratabound gold deposit in Zhenfeng County, Guizhou Province. *Geol. China* **2006**, *33*, 169–177. (In Chinese) [CrossRef]
4. Wang, D.F. Preliminary Study on Geological and Geochemical Characteristics of Jiadi Gold Deposit in Panxian, Guizhou Province. Master's Thesis, Guizhou University, Guiyang, China, 2015; pp. 32–44. (In Chinese)

5. Chen, M.H.; Mao, J.W.; Qu, W.J.; Wu, L.L.; Uttley, P.J.; Norman, T.; Zheng, J.M.; Qin, Y.Z. Re-Os dating of arsenian pyrites from the Lannigou gold deposit, Zhenfeng, Guizhou Province, and its geological significances. *Geol. Rev.* **2007**, *53*, 371–382. (In Chinese) [CrossRef]

6. Xiao, D.Z. The Study on Ore-Forming Fluids in the Yata Carlin-Type Gold Deposit, Guizhou Province. Ph.D. Thesis, Chengdu University of Technology, Chengdu, China, 2012; pp. 37–43. (In Chinese)

7. Chen, M.H.; Mao, J.W.; Bierlein, F.P.; Norman, T.; Uttley, P.J. Structural features and metallogenesis of the Carlin-type Jinfeng (Lannigou) gold deposit, Guizhou Province, China. *Ore Geol. Rev.* **2011**, *43*, 217–234. [CrossRef]

8. Chen, M.H.; Huang, Q.W.; Li, J.X.; Jiang, B.C.; Zhang, C.M. Structure analysis and structural metallogenesis of the Linwang gold deposit, Leye, Guangxi, China. *Geotecton. Metallog.* **2010**, *34*, 349–361. (In Chinese) [CrossRef]

9. Wu, S.Y.; Hou, L.; Ding, J.; Wu, W.; Qin, K.; Zhang, J.R.; Zhu, S.B. Ore-controlling structure types and characteristics of ore-forming fluid of the Carlin-type gold orefield in southwestern Guizhou, China. *Acta Petrol. Sin.* **2016**, *32*, 2407–2424. (In Chinese)

10. Berger, B.R.; Tingley, J.V.; Drew, L.J. Structural localization and origin of compartmentalized fluid flow, Comstock Lode, Virginia City, Nevada. *Econ. Geol.* **2003**, *98*, 387–408. [CrossRef]

11. Simmons, S.F.; Brown, K.L. Gold in magmatic hydrothermal solutions and the rapid formation of a giant ore deposit. *Science* **2006**, *314*, 288–291. [CrossRef]

12. Zhai, Y.S. Some preblems on the study of ore field structures. *Geol. Rev.* **1984**, *30*, 19–25. (In Chinese)

13. He, J.P.; Yuan, S.F.; Wang, X.Y.; Pian, H.Y. Geochemical Characteristics of the Lianhuashan Anticline in the Southwest Guizhou Dense Area of Mineral Deposits. *Acta Geol. Sichuan* **2018**, *38*, 384–397. [CrossRef]

14. Zeng, G.P.; Luo, D.W.; Gong, Y.J.; Hu, X.L.; Li, H. Structures and implications for fluid migration in the Jiadi Carlin-type gold deposit, Guizhou Province, Southwest China. *Resour. Geol.* **2018**, *68*, 373–394. [CrossRef]

15. Xia, Y.; Zhang, Y.; Su, W.C.; Tao, Y.; Zhang, X.C.; Liu, J.Z.; Deng, Y.M. Metallogenic model and prognosis of the Shuiyindong super-large stratabound Carlin-type gold deposit, Southwestern Guizhou Province, China. *Acta Geol. Sin.* **2009**, *83*, 1473–1482. (In Chinese) [CrossRef]

16. Li, B.H.; Gu, X.Y.; Fu, S.H.; Xu, S.H.; Chen, C.H.; Dong, S.Y. The evidence from fluid inclusions for the immiscibility of the ore-forming fluids in the Shuiyindong gold deposit, Guizhou Province. *Earth Sci. Front.* **2010**, *17*, 286–294. (In Chinese)

17. Peng, Y.W.; Gu, X.X.; Liu, L.; Cheng, W.B. Fluid inclusion characteristics and implications to mineralization in the Zimudang gold deposit in Southwest Guizhou Province, China. *Acta Mineral. Sin.* **2012**, *32*, 211–220. (In Chinese) [CrossRef]

18. Zhao, F.Y.; Xiao, C.G.; Zhang, B.Q.; Wang, S.H.; Li, J.H.; Ma, J. REE and isotopic features of the Jiadi gold deposit in Panxian county of Guizhou province and its ore-forming material source. *Geol. Explor.* **2018**, *54*, 465–478. (In Chinese)

19. Zeng, G.P. Study on the Structurally Controlling on the Micro-Disseminated Gold Deposits in the Western of the Southwest Guizhou Gold Ore Concentration Area. Ph.D. Thesis, China University of Geosciences, Wuhan, China, 2018; pp. 38–46.

20. Wang, D.H.; Chen, Y.C.; Tang, J.X.; Ying, L.J.; Wang, C.H.; Liu, S.B.; Li, L.X.; Qin, Y.; Li, H.Q.; Qu, W.J.; et al. New data of the rock-forming and ore-forming chronology for China's important mineral resources areas. *Acta Geol. Sin.* **2010**, *84*, 1030–1040. (In Chinese)

21. Xia, Y. Characteristics and Model for Shuiyindong Gold Deposit in Southwestern Guizhou, China. Ph.D. Thesis, Institute of Geochemistry, Chinese Academy of Sciences, Guiyang, China, 2005; pp. 36–50. (In Chinese)

22. Yan, D.P.; Zhou, M.F.; Song, H.L.; John, M. Where was South China located in the reconstruction of Rodinia? *Earth Sci. Front.* **2002**, *9*, 249–256. (In Chinese) [CrossRef]

23. Wu, F.Y.; Ge, W.C.; Sun, D.Y.; Guo, C.L. Discussions on the lithospheric thinning in Eastern China. *Earth Sci. Front.* **2003**, *10*, 51–60. (In Chinese)

24. Lehrmann, D.J.; Payne, J.L.; Pei, D.H.; Enos, P.; Druke, D.; Steffen, K.; Zhang, J.Y.; Wei, J.Y.; Orchard, M.J.; Ellwood, B. Record of the end-Permian extinction and Triassic biotic recovery in the Chongzuo-Pingguo platform, Southern Nanpanjiang basin, Guangxi, South China. *Palaeogeogr. Palaeoclimatol. Palaeoecol.* **2007**, *252*, 200–217. [CrossRef]

25. Hua, R.M.; Chen, P.R.; Zhang, W.L.; Lu, J.J. Three major metallogenic events in Mesozoic in South China. *Miner. Depos.* **2005**, *24*, 99–107. (In Chinese) [CrossRef]

26. Hu, Y.; Liu, W.; Wang, J.J.; Zhang, G.Q.; Zhou, Z.Z.; Han, R.S. Basin-scale structure control of Carlin-style gold deposits in central Southwestern Guizhou, China: Insights from seismic reflection profiles and gravity data. *Ore Geol. Rev.* **2017**, *91*, 444–462. [CrossRef]

27. Tian, C.; Zhang, W.G.; He, H.J.; Yang, X.K.; Han, K.; Wang, X.H. Mineralogical characteristics of gold-bearing pyrite and gold occurrence regularity of the Jiadi gold deposit in southwestern Guizhou Province. *Geol. China* **2020**, *1*, 1–19. (In Chinese)

28. Liu, J.Z.; Xia, Y.; Deng, Y.M.; Su, W.C.; Zhang, X.C.; Qiu, L.; Chen, M.; Chen, F.E.; Fu, Z.K. Researches on the Sbt of Shuiyindong gold deposit and significance for regional prospecting. *Gold Sci. Technol.* **2009**, *17*, 1–5. (In Chinese) [CrossRef]

29. Zhang, H.T.; Su, W.C.; Tian, J.J.; Liu, Y.P.; Liu, J.Z.; Liu, C.Q. The Occurrence of Gold at Shuiyindong Carlin-type Gold Deposit, Guizhou. *Acta Mineral. Sin.* **2008**, *1*, 17–24. [CrossRef]

30. Williams, P.F. Multiply deformed terrains—Problems of correlation. *J. Struct. Geol.* **1985**, *7*, 269–280. [CrossRef]

31. Allmendinger, R.W.; Cardozo, N.; Fisher, D. *Structural Geology Algorithms: Vectors and Tensors in Structural Geology*; Cambridge University Press: Cambridge, UK, 2012; pp. 36–50. [CrossRef]

32. Cao, H.S. A discussion on the environment and minerogenesis of "Dachang Strata" in Southwest Guizhou. *Guizhou Geol.* **1991**, *26*, 5–13. (In Chinese)

33. Li, J.H. The Study of Ore-Forming Processes of the Jiadi and Damaidi Basalt-Hosted Gold Deposits, Southwestern Guizhou Province, China. Ph.D. Thesis, Guizhou University, Guiyang, China, 2021; pp. 40–44. (In Chinese)

34. Li, X.G. Mesozoic structural Deformation Characteristics and Superposition Pattern in Southwest Guizhou, China. Master's Thesis, China University of Geosciences, Wuhan, China, 2012; pp. 30–38. (In Chinese)

35. Chen, Y.Z.; Yang, G.L.; Tang, Y. Characteristics of Meso-Cenozoic tectonic deformation and simulation of stress field in Southwest Guizhou Province. *Geotecton. Metallog.* **2021**, *45*, 667–680. (In Chinese) [CrossRef]

36. Wu, S.Y. The Study of Tectonic-Mmagmatic-Hydrothermal Metallogenic Model of Carlin-Type Gold Deposit in Southwestern Guizhou Province, Dr. Sci. Thesis, Chin. China University of Geosciences, Wuhan, China, 2019; pp. 52–61. (In Chinese)

37. Bao, Z.W.; Jayanta, G. Metallogeny of the Lannigou sedimentary rock-hosted disseminated gold deposit in Southwestern Guizhou Province, China. *Acta Geol. Sin.* **2007**, *81*, 121–134. [CrossRef]

38. Bao, T.; Ni, P.; Li, S.N.; Xiang, H.L.; Wang, G.G.; Chi, Z.; Li, W.S.; Ding, J.Y.; Dai, B.Z. Geological, fluid inclusion, and H–O–C–S–Pb isotopic constraints on the genesis of the Shuangqishan gold deposit, Fujian, China. *J. Geochem. Explor.* **2020**, *214*, 106–544. [CrossRef]

39. Huang, G.W.; Pan, J.Y.; Xia, F.; Yan, J.; Zhang, C.Y.; Wu, D.H.; Liu, Y. Provenance of uranium mineralization of the Yuqia area, Northwest China: Constraints from detrital zircon U-Pb geochronology and Hf isotopes. *J. Earth Sci.* **2022**, *33*, 1549–1570. [CrossRef]

40. Zhang, X.T.; Pan, J.Y.; Xia, F. Fluid inclusion constraints on ore-forming mechanism of Lujing uranium deposit in Jiangxi-Hunan border region. *Earth Sci.* **2021**, *47*, 1–21. (In Chinese) [CrossRef]

41. Li, B.H.; Gu, X.X.; Li, L.; Xu, S.H.; Fu, S.H.; Chen, C.H.; Dong, S.Y. The effect of CO_2-H_2O fluid immiscibility on the solubility of Au: A case study of the Shuiyindong gold deposit, Zhenfeng County, Guizhou Province. *Geol. Bull. China* **2011**, *30*, 766–772. (In Chinese) [CrossRef]

42. Lu, H.Z. Role of CO_2 fluid in the formation of gold deposits: Fluid inclusion evidences. *Geochimica* **2008**, *37*, 321–328. (In Chinese) [CrossRef]

43. Qiu, L.F.; Wu, D.; Wu, Y.; Jin, G.S.; Han, J.; Liu, J.G.; Guo, J. Characteristics of ore-forming fluids and sources of polymetallic ore-forming materials in deep segment of uranium deposits in Niutoushan area, Xiangshan. *Miner. Depos.* **2019**, *38*, 291–302. (In Chinese) [CrossRef]

44. Yao, J. Studies on Ore-Forming Material Source and Ore Genesis of Laozhaiwan Fine-Disseminated Gold Deposit, Yunnan, China. Ph.D. Thesis, Chengdu University of Technology, Chengdu, China, 2008; pp. 35–45. (In Chinese)

45. Xue, C.D.; Han, R.S.; Yang, H.L.; Yang, Z.M.; Tian, S.H.; Liu, Y.Q.; Hao, B.W. Isotope geochemical evidence for ore-forming fluid resources in Hetaoping Pb-Zn deposit, Baoshan, Northwestern Yunnan. *Miner. Depos.* **2008**, *2*, 243–252. [CrossRef]

46. Jin, X.Y. Geology, Mineralization and Genesis of the Nibao, Shuiyindong and Yata Gold Deposits in SW Guizhou Province, China. Ph.D. Thesis, China University of Geosciences, Wuhan, China, 2017; pp. 38–56. (In Chinese)

47. Clayton, P.J.; Halikas, J.A.; Maurice, W.L. The depression of widowhood. *Br. J. Psychiatry J. Ment. Sci.* **1972**, *120*, 71–78. [CrossRef]

48. Peng, Y.W.; Gu, X.X.; Zhang, Y.M.; Liu, L.; Wu, C.Y.; Chen, S.Y. Source and evolution of ore-forming fluid of the Huijiabao gold field, Southwestern Guizhou: Evidences from fluid inclusions and stable isotopes. *Bull. Mineral. Petrol. Geochem.* **2014**, *33*, 666–680. (In Chinese) [CrossRef]

49. Zhang, L.G.; Chen, Z.S.; Liu, J.X.; Yu, G.X.; Wang, K.F. *Two Stage Water Rock Isotope Exchange Theory and Its Exploration Application*; Geological Publishing House: Beijing, China, 1995; pp. 30–50.

50. Sheppard, S.M.F. Characterization and isotopic variations in natural waters. *Rev. Mineral.* **1986**, *16*, 165–183. [CrossRef]

51. Taylor, B.E. Stable Isotope Geochemistry of Ore-Forming Fluids. In *Short Course in Stable Isotope Geochemistry of Low Temperature Fluids*; Kyser, T.K., Ed.; Mineralogical Association of Canada: Quebec, Canada, 1987; pp. 28–40.

52. Hu, R.Z.; Su, W.C.; Bi, X.W.; Tu, G.Z.; Hofstra, A.H. Geology and geochemistry of Carlin-type gold deposits in China. *Miner. Depos.* **2002**, *37*, 378–392. [CrossRef]

53. Large, S.J.E.; Bakker, E.Y.N.; Weis, P.; Walle, M.; Heinrich, C.A. Trace elements in fluid inclusions of sediment-hosted gold deposits indicate a magmatic-hydrothermal origin of the Carlin ore trend. *Geology* **2016**, *44*, 1015–1018. [CrossRef]

54. Roedder, E. *Fluid Inclusions: Reviews in Mineralogy*; Mineral Society of America: Washington, DC, USA, 1984; Volume 12, pp. 1–644.

55. Su, W.; Zhang, H.; Hu, R.; Xi, G.; Xia, B.; Chen, Y.; Chen, Z. Mineralogy and geochemistry of gold-bearing arsenian pyrite from the Shuiyindong Carlin-type gold deposit, Guizhou, China: Implications for gold depositional processes. *Miner. Depos.* **2011**, *47*, 653–662. [CrossRef]

56. Zhuo, Y.Z.; Hu, R.Z.; Xiao, J.F.; Zhao, C.H.; Huang, Y.; Yan, J.; Li, J.W.; Gao, W.; Li, J.X. Trace elements and C-O isotopes of calcite from Carlin-type gold deposits in the Youjiang Basin, China: Constraints on ore-forming fluid compositions and sources. *Ore Geol. Rev.* **2019**, *113*, 103–167. [CrossRef]

57. Zhou, L.; Hu, Y.Z.; Tan, X.L.; Li, P.Y.; Cheng, Y. Basin-scale structure of Puan Pb-Zn deposit area, Southwest Guizhou, China. *Earth Sci.* **2022**, *47*, 368–386. (In Chinese)

58. Zheng, S.; Hu, Y.Z.; Guan, S.J.; Liu, X.X. Structural deformation and evolution of the Lannigou gold ore-field in Southwestern Guizhou. *Geol. Rev.* **2020**, *66*, 1431–1445. (In Chinese) [CrossRef]

59. Goldfarb, R.J.; Taylor, R.D.; Collins, G.S.; Goryachev, N.A.; Orlandini, O.F. Phanerozoic continental growth and gold metallogeny of Asia. *Gondwana Res.* **2014**, *25*, 48–102. [CrossRef]

60. Chen, B.J. Seismic activity and continental dynamic background in Southwestern Guizhou and its adjacent region. *J. Geol. Geodyn.* **2009**, *29*, 53–58. (In Chinese) [CrossRef]

61. Han, Z.Y.; Liang, B.; Zhong, C.H. Geochemical Characteristics of the Pb-Zn Deposits in the Ningnan Area. *Acta Geol. Sichuan* **2018**, *38*, 384–397. (In Chinese)

62. Su, W.; Xia, B.; Zhang, H.; Zhang, X.C.; Hu, R.Z. Visible gold in arsenian pyrite at the Shuiyindong Carlin-type gold deposit, Guizhou, China: Implications for the environment and processes of ore formation. *Ore Geol. Rev.* **2008**, *33*, 667–679. [CrossRef]